

## Article

# The Effect of Ignition Timing on the Emission and Combustion Characteristics for a Hydrogen-Fuelled ORP Engine at Lean-Burn Conditions

Junfeng Huang <sup>1</sup>, Jianbing Gao <sup>1,\*</sup> , Ce Yang <sup>1</sup>, Guohong Tian <sup>2</sup> and Chaochen Ma <sup>1</sup><sup>1</sup> School of Mechanical Engineering, Beijing Institute of Technology, Beijing 100081, China<sup>2</sup> Department of Mechanical Engineering Sciences, University of Surrey, Guildford GU2 7XH, UK

\* Correspondence: gaojianbing@bit.edu.cn

**Abstract:** The application of hydrogen fuel in ORP engines makes the engine power density much higher than that of a reciprocating engine. This paper investigated the impacts of combustion characteristics, energy loss, and NO<sub>x</sub> emissions of a hydrogen-fuelled ORP engine by ignition timing over various equivalence ratios using a simulation approach based on FLUENT code without considering experiments. The simulations were conducted under the equivalence ratio of 0.5~0.9 and ignition timing of  $-20.8\sim-8.3^\circ$  CA before top dead centre (TDC). The engine was operated under 1000 RPM and wide-open throttle condition which was around the maximum engine torque. The results indicated that significant early ignition of the ORP engine restrained the flame development in combustion chambers due to the special relative positions of ignition systems to combustion chambers. In-cylinder pressure evolutions were insensitive to early ignition. The start of combustion was the earliest over the ignition timing of  $-17.3^\circ$  CA for individual equivalence ratios; the correlations of the combustion durations and equivalence ratios were dependent on the ignition timing. Combustion durations were less sensitive to equivalence ratios in the ignition timing range of  $-14.2\sim-11.1^\circ$  CA before TDC. The minimum and maximum heat release rates were  $15\text{ J}\cdot(\text{^\circ CA})^{-1}$  and  $22\text{ J}\cdot(\text{^\circ CA})^{-1}$  over the equivalence ratios of 0.5 and 0.9, respectively. Indicated thermal efficiency was higher than 41% for early ignition scenarios, and it was significantly affected by late ignition. Energy loss by cylinder walls and exhaust was in the range of 10~16% and 42~58% of the total fuel energy, respectively. The impacts of equivalence ratios on NO<sub>x</sub> emission factors were affected by ignition timing.

**Keywords:** opposed rotary piston engines; high power density; lean-burn characteristics; ignition timing; energy loss; nitrogen oxides



**Citation:** Huang, J.; Gao, J.; Yang, C.; Tian, G.; Ma, C. The Effect of Ignition Timing on the Emission and Combustion Characteristics for a Hydrogen-Fuelled ORP Engine at Lean-Burn Conditions. *Processes* **2022**, *10*, 1534. <https://doi.org/10.3390/pr10081534>

Academic Editors: Alessandro D'Adamo and Fabrizio Scala

Received: 8 July 2022

Accepted: 3 August 2022

Published: 5 August 2022

**Publisher's Note:** MDPI stays neutral with regard to jurisdictional claims in published maps and institutional affiliations.



**Copyright:** © 2022 by the authors. Licensee MDPI, Basel, Switzerland. This article is an open access article distributed under the terms and conditions of the Creative Commons Attribution (CC BY) license (<https://creativecommons.org/licenses/by/4.0/>).

## 1. Introduction

With the increasing number of automobiles, large amounts of fossil fuels are consumed annually, leading to much carbon dioxide (CO<sub>2</sub>) and hazardous pollutants being emitted into the atmosphere. Exhaust emissions from automobiles have caused serious problems for the environment and human health, such as global warming [1,2] and respiratory diseases [3]. The exhaust emissions were seriously worsened by the cold start and warm-up process due to the low efficiency of after-treatment [4]. Hybrid vehicles and range-extended electric vehicles, as the transitions from internal combustion engine vehicles to pure electric vehicles, are attracting increasing attention [5] for their ability to drop CO<sub>2</sub> and hazardous emissions. The power sources of hybrid vehicles and range-extended electric vehicles are dominated by reciprocating engines [6] and Wankel engines [7]. Opposed rotary piston (ORP) engines [8], as a new type of internal combustion engines, have the advantages of high power density and few moving components which are the characteristics of ideal power sources for hybrid vehicles and range-extended electric vehicles [9].

Much research has been done regarding reciprocating engines and Wankel engines to enhance thermal efficiency and to decrease exhaust emissions [10–15]. Compared with

reciprocating engines, Wankel engines have fewer moving parts and are free of complex connecting-rod mechanisms [16]; however, hydrocarbon (HC) and carbon monoxide (CO) emissions of Wankel engines are much higher than reciprocating engines, due to severe quenching and crevice effects resulting from their narrow and long combustion chambers [17].

With regards to the investigations of ORP engines, the operation theory was firstly analyzed using mathematical equations [18,19]; additionally, the engine power output was considered to be linearly increased with cylinder numbers, resulting from the increased engine displacement; however, the combustion process was neglected in mathematical equations that more cylinders meant less time for each stroke during operation over the given engine speed; it would cause low volumetric efficiency, poor combustion efficiency and thermal efficiency, as well as much unburned fuel. Pan et al. [20] further investigated the leakages of the ORP engine, showing that increasing the engine speed and dropping compression ratio helped alleviate gas leakages. Gao et al. [21] compared the performance of a four-cylinder ORP engine with a reciprocating engine having the same displacement using numerical simulation methods. The maximum power output density was approximately 80 kW/L under naturally aspirated conditions for the gasoline fuelled ORP engine, and the power density was almost double of the reciprocating engines. With regards to ORP engines, the combustion process was different from reciprocating engines and Wankel engines due to the short cyclic period in time and special operations.

In order to drop CO<sub>2</sub> emissions, many types of alternative fuels such as natural gas [22], liquefied petroleum gas [23], methanol [24,25], ethanol [26], n-butanol [27], biodiesel [28], di-methyl carbonate [29] and hydrogen [30,31] have been applied to internal combustion engines. Hydrogen is considered to be an ultimate fuel due to non-pollutants combustion in theory [32,33]; additionally, hydrogen fuel has a higher energy density by mass compared with other fuels [34,35]. Hydrogen applications in internal combustion engines effectively decrease CO<sub>2</sub> emissions and hazardous pollutants and increase brake thermal efficiency [36,37] due to high flame propagation speed and small quenching distances [38,39]. Hydrogen is mainly produced from fossil and renewable biomass resources including reforming and pyrolysis. Currently, hydrogen has to be stored in a high-pressure tank. The density by volume is still much smaller than gasoline for high-pressure tank storage although the cost is low. In order to inject hydrogen into intake pipes or cylinders, a set of hydrogen delivery systems is necessary.

Du et al. [40] demonstrated that HC and CO emissions dropped when hydrogen fuel was directly injected into cylinders; meantime, the emission drops were dependent on the exhaust gas recirculation (EGR) rates; however, NO<sub>x</sub> emissions increased significantly by hydrogen additions due to higher in-cylinder combustion temperature. Gong et al. [41] indicated that 3 vol.% hydrogen additions in methanol expanded the lean-burn limits from an excess air ratio of 1.6 to 2.2 for a reciprocating spark ignition engine, which would benefit from HC emission reductions (engine speed of 1800 RPM and intake manifold pressure of 0.68 bar); Additionally, lean-burn dropped NO<sub>x</sub> and soot formations simultaneously; it was also demonstrated that hydrogen-enriched combustion could expand the lean-burn limits to excess air ratio of 2.9 for a medium compression ratio methanol spark ignition engine [42]. Yu et al. [43] proved that hydrogen additions combined with an optimized injection strategy could achieve an increase of 4.5% in brake thermal efficiency. Shi et al. [44] researched the impacts of hydrogen split direct injection on the performance of a gasoline/hydrogen-fuelled Wankel engine, indicating that thermal efficiency was significantly enhanced by wide durations of secondary injection. Split injection also achieved near-zero HC and CO emissions, although an increase in NO<sub>x</sub> emissions was observed.

Because of the high flame propagation speed, hydrogen combustion could further present the merits of ORP engines by shortening combustion durations. The performance of a hydrogen-fuelled ORP engine under wide open throttle conditions was investigated in previous work [9]. The results indicated that the start of combustion was late and the combustion durations were long over 5000 RPM engine speed, resulting in low indicated

thermal efficiency;  $\text{NO}_x$  emission factors over 1000 RPM were approximately five times of 5000 RPM scenario; it was mainly caused by higher combustion temperature and longer durations for low engine speed, contributing to  $\text{NO}_x$  formations. The indicated power density was approximately 70 kW/L, which was approximately 15% lower than that of gasoline scenarios due to less air suction under naturally aspirated conditions.

When a turbocharger was applied to the hydrogen ORP engine, the power density was increased to approximately 104 kW/L, and the volumetric efficiency was higher than 89.5% even for the engine speed of 5000 RPM [45]; however,  $\text{NO}_x$  emission factors reached 14 g/(kW·h) over low engine speeds [45]. Equivalence ratios of 0.7~0.8 could significantly drop  $\text{NO}_x$  emission factors, with a minor penalty of indicated thermal efficiency [46]. Regarding dropping  $\text{NO}_x$  emission factors using lean-burn technology, naturally aspirated engines presented better performance than turbocharged engines [47]. Further, the optimal ignition timing under various engine load conditions was explored [48,49]. The results indicated that the optimal ignition timing was insensitive to the engine load and speed due to the existence of cylinder bowls. The optimal ignition timing was at the positions where the bottom of spark plugs was in the centres of the bowl surfaces, being benefited from more flame propagation directions.

Investigations of ORP engines are at an early stage, especially for hydrogen applications, such that many issues are remained to be addressed although they have a high potential of applying to hybrid vehicles and range-extended electric vehicles. As for the hydrogen-fuelled internal combustion engines, lean-burn was effective to suppress the  $\text{NO}_x$  formations; meantime, the combustion characteristics were changed accordingly such as the heat release rates, and combustion durations, leading to the variations of optimal ignition timing in terms of thermal efficiency. To the authors' knowledge, there are not any papers reporting the effect of ignition timing on hydrogen ORP engine performance under lean-burn conditions. In the meantime, the relationships between equivalence ratios and optimal ignition timing for the hydrogen ORP engines may be different from reciprocating engines and Wankel engines due to the special structure of combustion chambers. Improper ignition timing such as early ignition and late ignition may limit the flame propagations from spark plug regions to others in combustion chambers of ORP engines, even for the failure of ignition events.

The novelty and the main contributions of this paper to the existing literature include: (a) the combustion characteristics of the ORP engine under the combined effect of injection timing and equivalence ratios; (b) the effect of equivalence ratios (<1) on the optimal ignition timing in terms of thermal efficiency; (c)  $\text{NO}_x$  formations and energy loss by the joint impacts of ignition timing and equivalence ratios (<1); (d) how do the cylinder bowls affect the relationships between ignition timing and engine performance under lean-burn conditions.

## 2. Materials and Method

In this section, descriptions of the configurations and operation theory of the ORP engine are given; additionally, the simulation model and scenarios are provided.

### 2.1. Configurations and Operation Theory of the Opposed Rotary Piston Engine

The opposed rotary piston engine in this investigation is a four-cylinder, four-stroke spark ignition, and naturally aspirated engine. Configurations of this opposed rotary piston engine are shown in Figure 1 this engine includes four pistons, three intake pipes, two engine blocks, two shafts, two spark plugs, and one exhaust port. Each two pistons are connected with a shaft, as shown in Figure 1c,e. The engine operation process includes intake stroke, compression stroke, expansion stroke, and exhaust stroke, which is achieved by the relative movements of two adjacent pistons, as shown in Video 1 (from [45]). The rotation profiles of the two shafts are presented in the authors' previous work [21] that their rotation speeds are in analogous sinusoidal shapes, and their corresponding pistons have the same movements. During the engine operation process, the intake ports are opened

sequentially by the pistons. The operation principles of this ORP engine are shown in Figure S1 where the four piston movements and corresponding cylinder fluid domains are given. In the operation process, the volume evolutions of each two opposed cylinders are the same. More descriptions of this new engine are presented in Support Information.

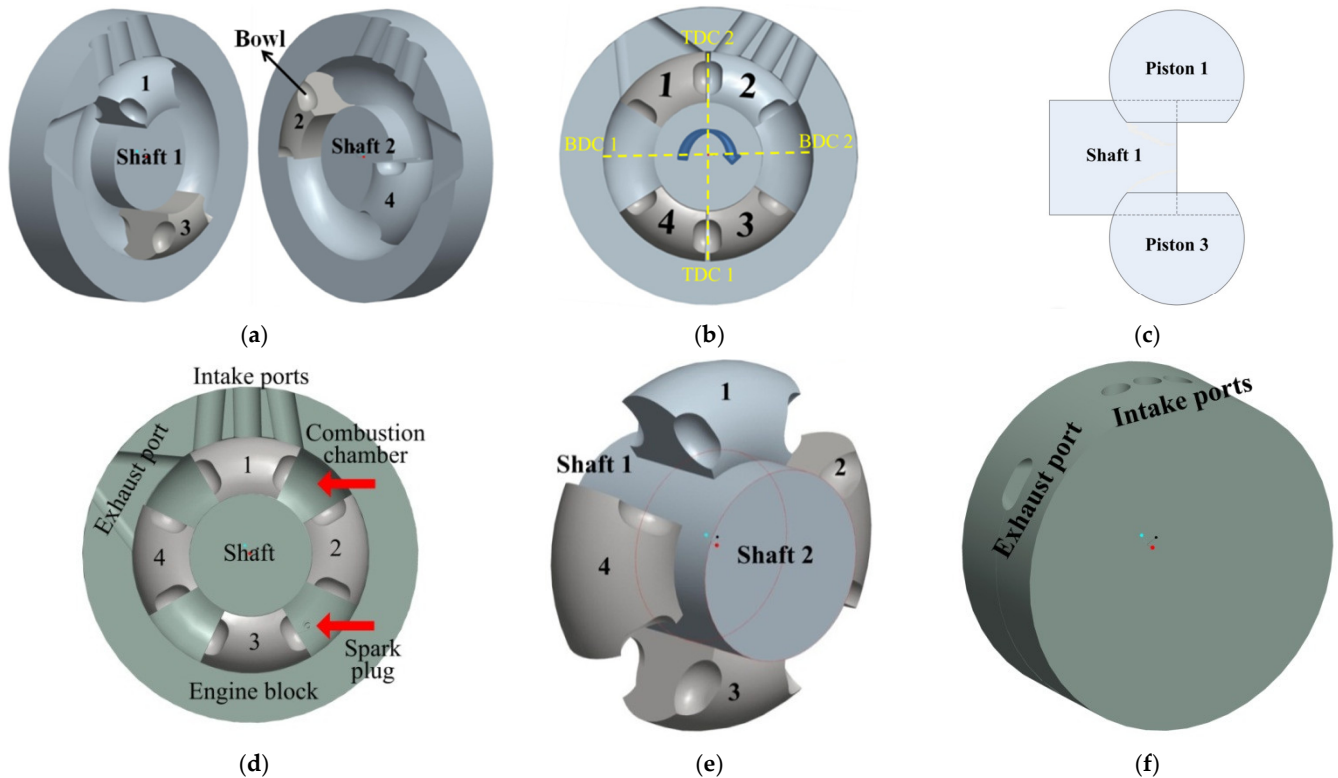


**Figure 1.** Configurations of the opposed rotary piston engine, from previous work [45]. (a) Relative positions of engine parts. (b) TDCs and BDCs. (c) Sketch of connectivity for pistons and shaft. (d) Relative positions of engine parts. (e) Pistons and shafts connections. (f) Engine blocks.

## 2.2. Merits Analysis of This Opposed Rotary Piston Engine

The structures of this ORP engine are completely different from reciprocating engines. As a new engine type, the merits of this ORP engine are as follows from the perspective of its structures: (1) it has high power density due to a short cyclic period of  $360^\circ$  CA; (2) volumetric efficiency is high, being benefited from the large area of intake and exhaust ports because of the separations of intake pipes, exhaust pipes, and spark plugs; (3)  $\text{NO}_x$  emissions are lower than conventional piston engines because of its short durations in time of high temperature; (4) engine knock possibility is low due to the separations of combustion chambers, spark plugs, and exhaust port; (5) the bowls in the pistons significantly can enlarge the range of ignition timing; (6) the structures of the intake and exhaust pipes drop the possibility of early ignition and backfire, especially for hydrogen fuel applications; (7) this engine has a compact design, is free of connecting rod mechanisms, and operates smoothly.

## 2.3. Computational Fluid Model

3D simulations in this work are conducted using FLUENT software. Dynamic meshes are used due to the changes in cylinder volume in the engine operation process. Because the investigation of this ORP engine is at an early stage, the fluid leakages are neglected in the simulations. Figure 2 shows the fluid domains and the meshes of engine components, and hexahedral meshes are applied. Regarding the overall mesh quality, the minimum orthogonal, maximum ortho skew, and maximum aspect ratio of the meshes are 0.337, 0.663 and 16.726, respectively. Sensitivity analysis of mesh numbers (size) and calculation

residuals are shown in Table S1. As can be seen, the mesh numbers and calculation residuals show limited impacts on the calculation results among the given scenarios. In this work, a total mesh number of 779,324 and calculation residuals of  $10^{-6}$  are used. The corresponding mesh numbers of engine parts is presented in the authors' previous work [9].

In this numerical simulation model, k-epsilon Re-Normalisation Group (RNG) viscous, species transport model, and finite-rate/Eddy-dissipation model are set in the FLUENT code [50].  $\text{NO}_x$  formations in FLUENT code are based on Zeldovitch mechanism [51]. There are some hypotheses in the simulation: (1) there are not any leakages between the pistons and engine blocks and shafts; (2) hydrogen–air mixture is completely homogeneous; (3) pressure drop from air filter is neglected; it means the intake pipe pressure is atmosphere pressure; (4) ignition position is the bottom of spark plugs.

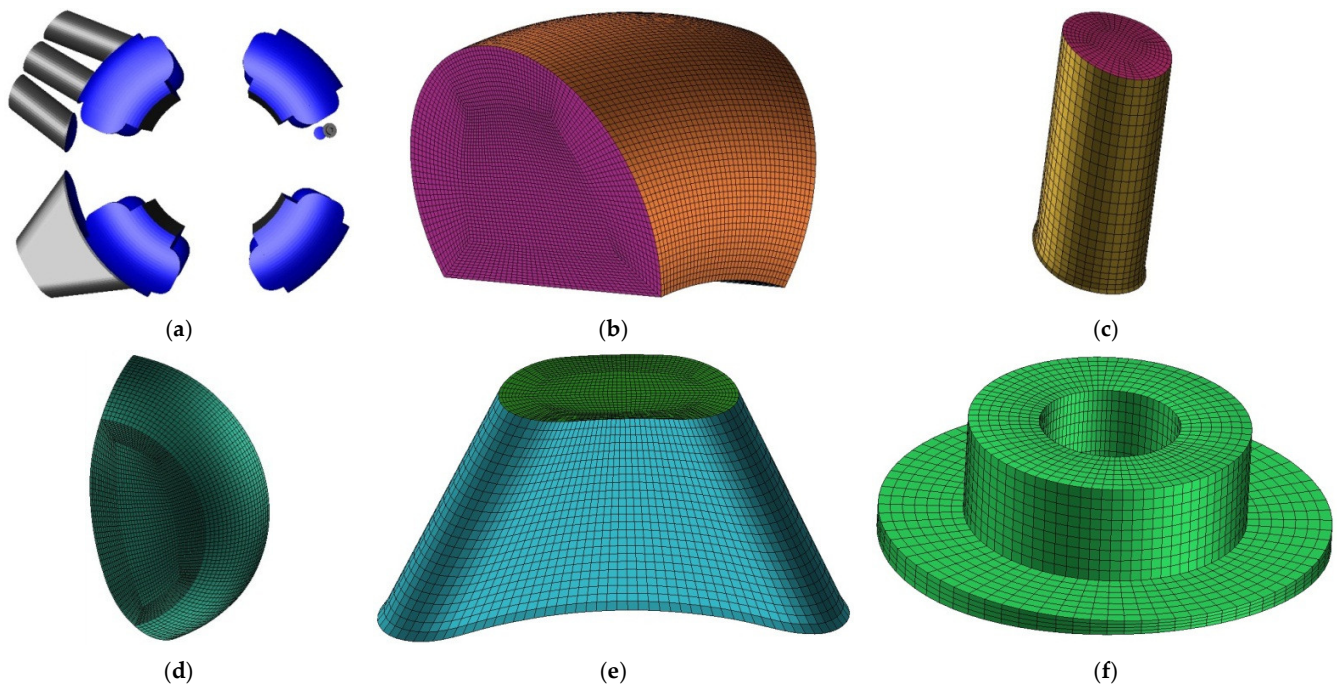


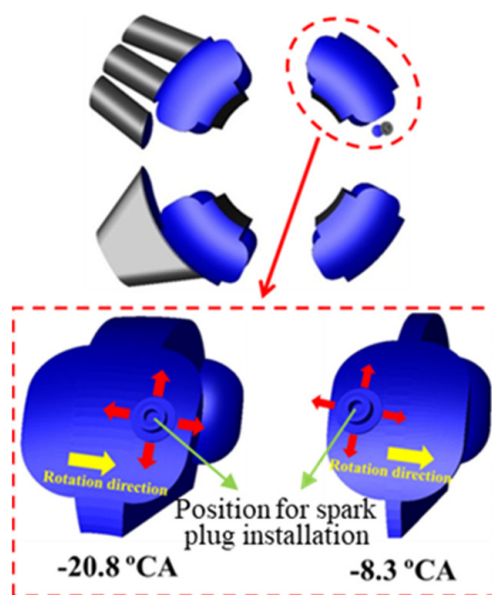
**Figure 2.** Computational fluid domains and meshes of the opposed rotary piston engine model. (a) Fluid domains. (b) Piston mesh. (c) Intake pipe mesh. (d) Bowl mesh. (e) Outlet pipe mesh. (f) Spark plug mesh.

#### 2.4. Boundary Condition Descriptions of the Scenarios

Since this work investigates the ignition timing impacts on the engine performance over the lean-burn conditions. The boundary condition settings of the simulation scenarios are shown in Table 1. As the rotation speed of the pistons is in analogous sinusoidal modes, the intervals in crank angle for each time step are different. The ignition timing settings of the simulation model are based on time steps. The equivalence ratios are in the range of 0.5~0.9, with an interval of 0.1. Ignition duration and ignition energy are 0.2 ms and 2 mJ, respectively. The relative positions of the combustion chambers and spark plugs are shown in Figure 3. As can be seen, there is an effective ignition timing range, beyond which the ignition will be a failure. Regarding the early and late ignition, flame propagation directions are limited by the walls of the bowls; it is completely different from reciprocating engines where the effective ignition is in a large scale although it generates significant negative impacts by improper ignition timing.

**Table 1.** Boundary condition settings of simulation scenarios.

Scenarios	1~5	6~10	11~15	16~20	21~25
Equivalence ratio (ER)	0.5	0.6	0.7	0.8	0.9
Rotation speed/RPM	1000				
Throttle opening/%	100%				
Intake pressure/bar	1.0				
Intake temperature/K	293				
Cylinder wall temperature/K	573				
Outlet pressure/bar	1.0				
Fuel type	H <sub>2</sub>				
Time step size/ $\times 10^{-5}$ s	6.0				
Time steps per cycle	1000				
Ignition timing (time step)/ °CA after TDC	−20.8 (1060); −17.3 (1070); −14.2 (1080); −11.1 (1090); −8.3 (1100)				

**Figure 3.** Relative positions of spark plugs and combustion chambers.

### 3. Results and Discussion

In order to assess the performance of this hydrogen-fuelled ORP engine over various equivalence ratios and ignition timing, combustion characteristics, energy loss, and NO<sub>x</sub> emissions were reported in this section.

#### 3.1. Combustion Characteristics

Engine power output was significantly affected by pressure evolutions of combustion chambers. Rapid and early increases of the in-cylinder pressure at the start of combustion (end of compression stroke) would lead to much energy loss; however, the slow increase rates led to low peak in-cylinder pressure and high discharge pressure. Both aspects would lead to low thermal efficiency and power output. Figure 4 shows the in-cylinder pressure evolutions over various ignition timing and equivalence ratios; meantime, the peak in-cylinder pressure is shown in Figure S2. Peak in-cylinder pressure was less sensitive to early ignition than late ignition for this ORP engine due to the special relative positions of spark plugs and combustion chambers. The maximum difference of peak in-cylinder pressure among various equivalence ratios occurred at the ignition timing of  $-17.3^\circ$  CA. Regarding the scenarios over the same equivalence ratios, ignition timing of  $-17.3^\circ$  CA presented the highest peak in-cylinder pressure. Both early ignition and late ignition deviating from the proper ignition timing would lead to fewer flame propagation directions (see Figure 3).

Fewer flame propagation directions would drop the hydrogen combustion rates and in-cylinder pressure. Ignition timing of  $-17.3^\circ$  CA corresponded to the centre of both bowl surfaces where the hydrogen flame had more propagation directions than others.

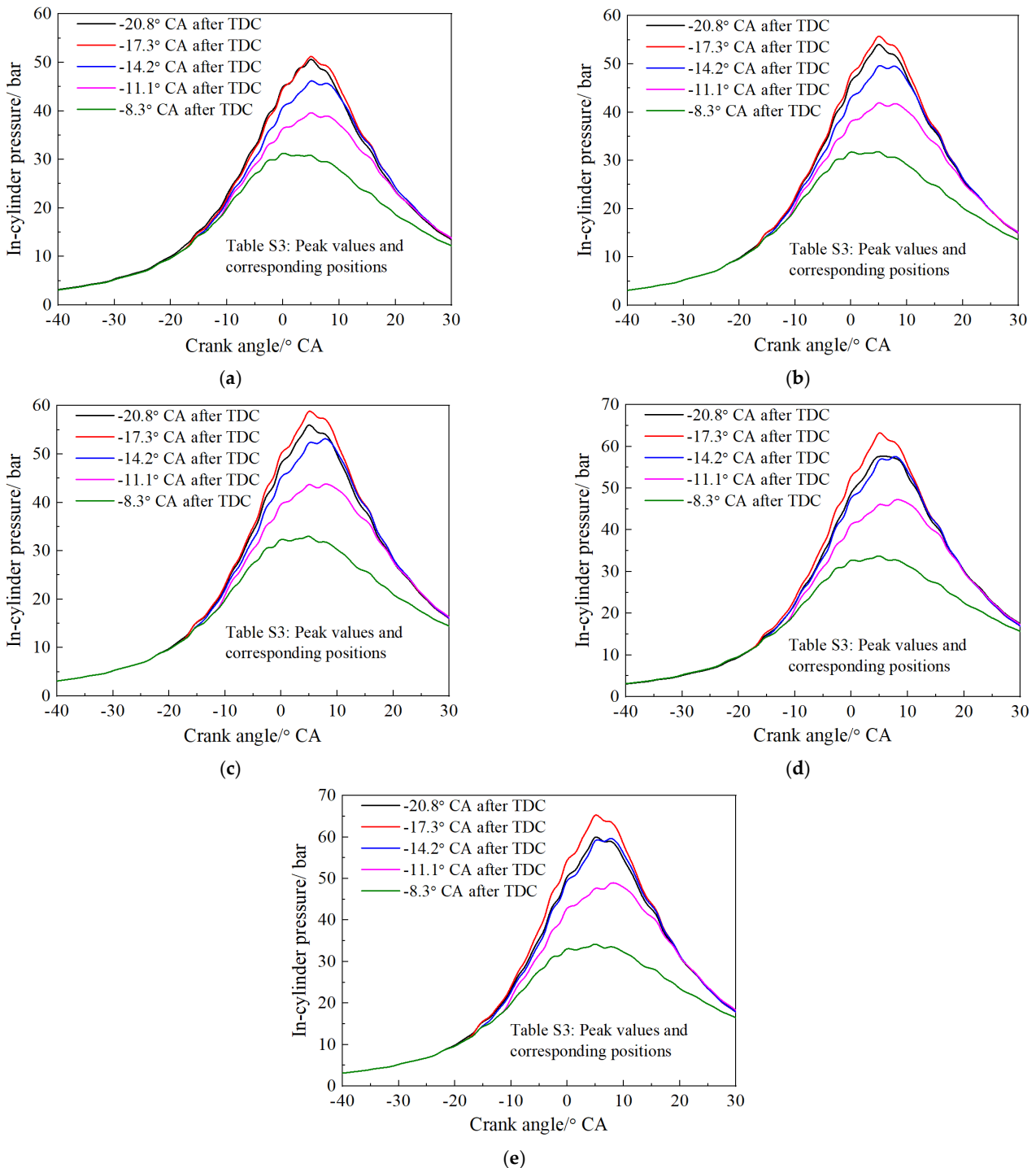


**Figure 4.** In-cylinder pressure evolutions over various equivalence ratios and ignition timing. (a) ER: 0.5. (b) ER: 0.6. (c) ER: 0.7. (d) ER: 0.8. (e) ER: 0.9.

Main differences of the impacts on in-cylinder pressure evolutions by ignition timing for ORP engines and other types of engines (reciprocating engines and Wankel engines) were caused by the special structures of combustion chambers. Significant advanced or retarded ignition timing limited the development of the hydrogen flame in combustion chambers, with fewer flame propagation directions (see Figure 3). Crank angle corre-

sponding to the peak in-cylinder pressure changed slightly over the ignition timing of  $-20.8^{\circ}$  CA $\sim$  $-11.1^{\circ}$  CA for this ORP engine; however, it was significantly advanced by the ignition timing of  $-8.3^{\circ}$  CA. The crank angle corresponding to the peak in-cylinder pressure was insensitive to the equivalence ratios, being around  $13^{\circ}$  CA after TDC for a turbocharged hydrogen engine [52], which was consistent with the simulation results of this hydrogen ORP engine.

In-cylinder pressure at the end of the expansion stroke was increased by increasing equivalence ratios (see Figure 5), which was caused by more hydrogen mass delivery over higher equivalence ratios. More hydrogen delivery in this work led to higher peak in-cylinder pressure; in the meantime, it caused more hydrogen (in mass) to combust in the second half period of expansion stroke. The pressure was higher than 4.0 bar at the equivalence ratio of 0.9; however, it was lower than 3.6 bar at the equivalence ratio of 0.5. The lowest pressure at the end of expansion stroke corresponded to the ignition timing of  $-17.3^{\circ}$  CA $\sim$  $-14.2^{\circ}$  CA over individual equivalence ratio scenarios. Regarding naturally aspirated engines, higher pressure at the end of expansion stroke meant more energy loss through the exhaust. P-V diagrams of the scenarios are shown in Figure S3. The main differences of P-V diagrams over various ignition timing were focused on the first half of the expansion stroke; the pressure differences were limited over the last half of the expansion stroke.

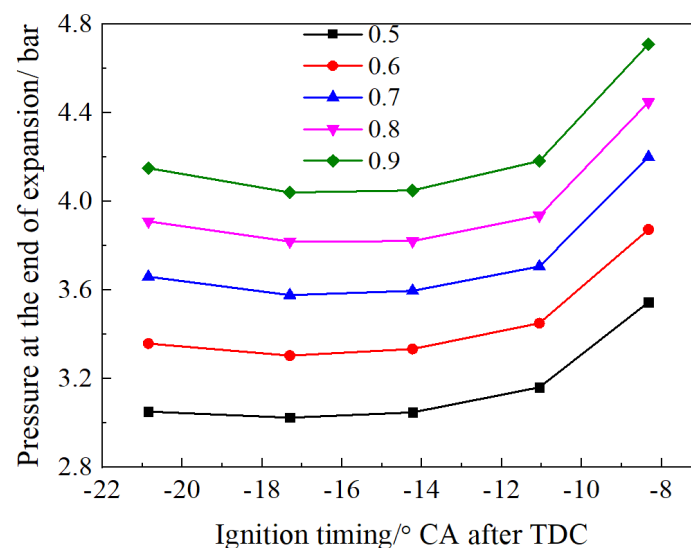


**Figure 5.** Pressure at the end of expansion stroke over various equivalence ratios and ignition timing.

Mass burn fraction profiles during combustion over various equivalence ratios and ignition timing are shown in Figure S4. Distinctions of the mass burn fraction profiles in the ignition timing of  $-20.8^{\circ}$  CA $\sim$  $-14.2^{\circ}$  CA were minor; however, they were significant for the range of  $-11.1^{\circ}$  CA $\sim$  $-8.3^{\circ}$  CA. Mass burn fraction profiles were retarded as a whole by late ignition for a spark ignition engine fuelled with syngas over the equivalence ratio of 0.85 [53]. Figure 6 shows the start of combustion, combustion phase, and combustion durations of the given cases. Start of combustion was advanced by increasing equivalence ratios over the same ignition timing scenarios. Start of combustion, combustion phase and combustion durations over the ignition timing of  $-17.3^{\circ}$  CA presented the lowest value for the individual equivalence ratio. Combustion durations over the equivalence ratio of 0.5 were the shortest over the ignition timing of  $-20.8^{\circ}$  CA; however, it was the longest over the ignition timing of  $-8.3^{\circ}$  CA. The joint actions of later ignition and less flame propagation led to the delayed combustion for the ignition timing of  $-8.3^{\circ}$  CA.

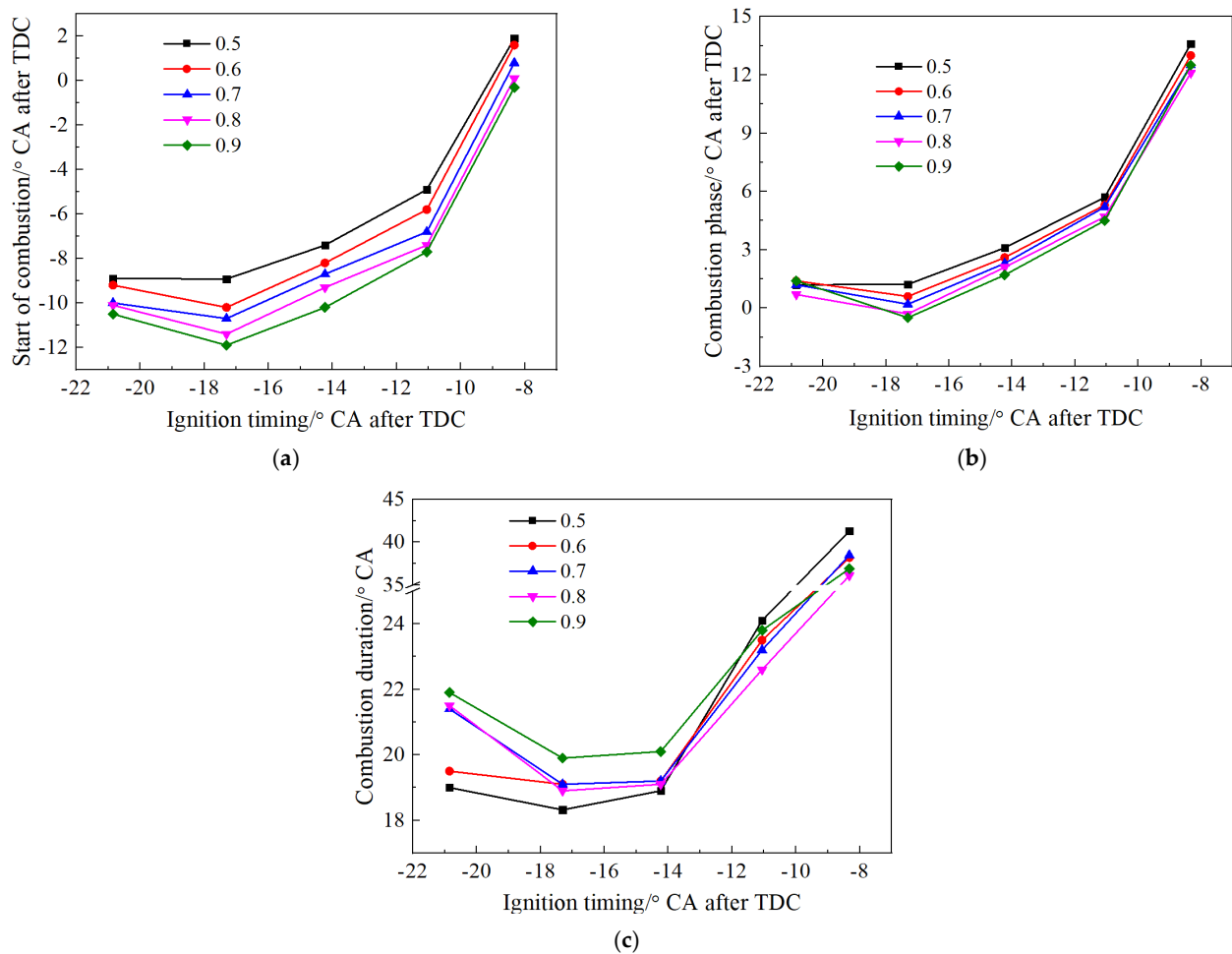


**Figure 6.** Start of combustion, combustion phase, and combustion durations over various equivalence ratios and ignition timing. (a) Start of combustion. (b) Combustion phase. (c) Combustion durations.

Heat release rates determined the in-cylinder pressure evolutions, further affecting the engine efficiency and power output. Accumulated heat release and heat release rates are shown in Figure 7. Heat release rates were dominated by the amounts of hydrogen fuel delivery, resulting in the drop of peak heat release rates with decreasing equivalence ratios. Maximum peak heat release rates were approximately  $15 \text{ J} \cdot (\text{°CA})^{-1}$  over the equivalence ratio of 0.5; and it reached  $22 \text{ J} \cdot (\text{°CA})^{-1}$  over the equivalence ratio of 0.9. Peak heat release rates for a hydrogen/natural gas engine were increased significantly by advancing ignition timing, and corresponding crank angle was also advanced [54]. The fluctuations were also observed, and the reasons were the same as the fluctuations in in-cylinder pressure.

One of the purposes of adjusting the ignition timing of internal combustion engines was to achieve high thermal efficiency for low fuel consumption. Indicated thermal efficiency over various equivalence ratios and ignition timing is shown in Figure 8. Indicated thermal efficiency increased with the drop of equivalence ratios over the same ignition timing, which was mainly caused by low energy loss due to low combustion temperature and low discharge pressure over low equivalence ratios. The ignition timing of  $-17.3^\circ \text{ CA}$  presented the highest indicated thermal efficiency under the same equivalence ratio conditions. The impacts of brake thermal efficiency by equivalence ratios would be different from that of indicated thermal efficiency because mechanical efficiency increased with engine power output for the same engine speed. When ignition timing was later than  $-14.2^\circ \text{ CA}$ , indicated thermal efficiency dropped significantly due to the retarded start of combustion and prolonged combustion durations. The drop of indicated thermal efficiency was approximately 10% compared to the optimal values when the ignition timing was

retarded to  $-8.3^\circ$  CA; additionally, the difference of indicated thermal efficiency caused by equivalence ratios was narrowed by late ignition. Later ignition timing showed more sensitive impacts on indicated thermal efficiency than earlier ignition. To achieve low fuel consumption, the ignition timing should be in the range of  $-20.8^\circ$  CA $\sim$  $-14.2^\circ$  CA for the given equivalence ratios.

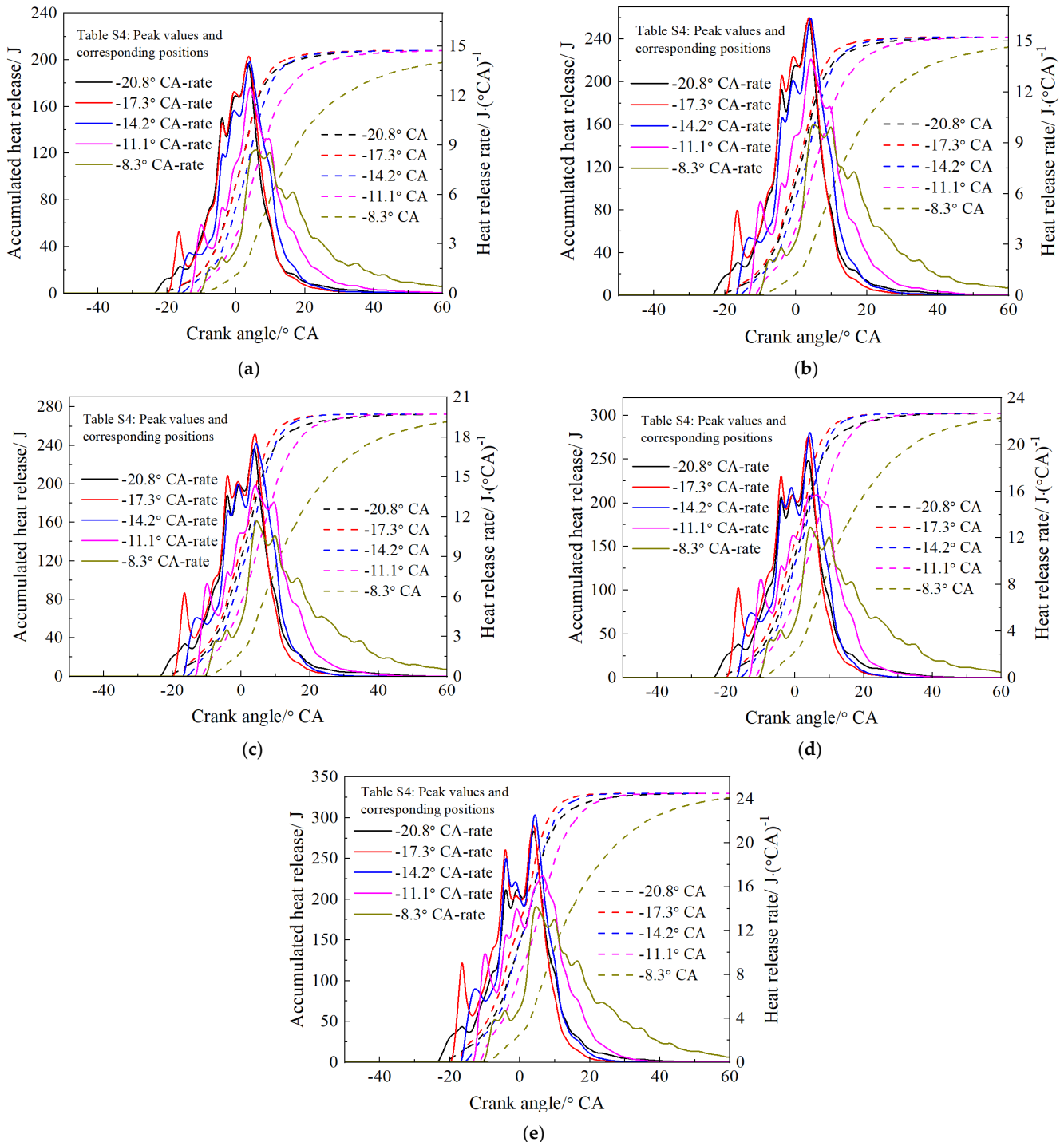


**Figure 7.** Accumulated heat release and heat release rates. (a) ER: 0.5. (b) ER: 0.6. (c) ER: 0.7. (d) ER: 0.8. (e) ER: 0.9.

In the authors' previous work [48,49], similar phenomenon was also observed over various load conditions that the indicated thermal efficiency had minor differences in the ignition timing range of  $-20.8^\circ$  CA $\sim$  $-14.2^\circ$  CA. Brake thermal efficiency and power

output of a hydrogen-fuelled reciprocating engine increased with equivalence ratios under lean-burn conditions [55]. The authors' simulation results agreed well with Sari et al. [56] that indicated thermal efficiency increased and then dropped with advancing ignition timing for a spark ignition engine fuelled with ethanol/water blended fuel; however, the main reasons of their correlations were different for reciprocating engines and ORP engines. For reciprocating engines, significant early ignition caused much energy loss (negative power in P-V diagrams) in the compression process, further lowering the thermal efficiency; however, it was caused by the limitations of flame development in combustion chambers for ORP engines because of the special relative positions of spark plugs to combustion chambers (see Figure 3).

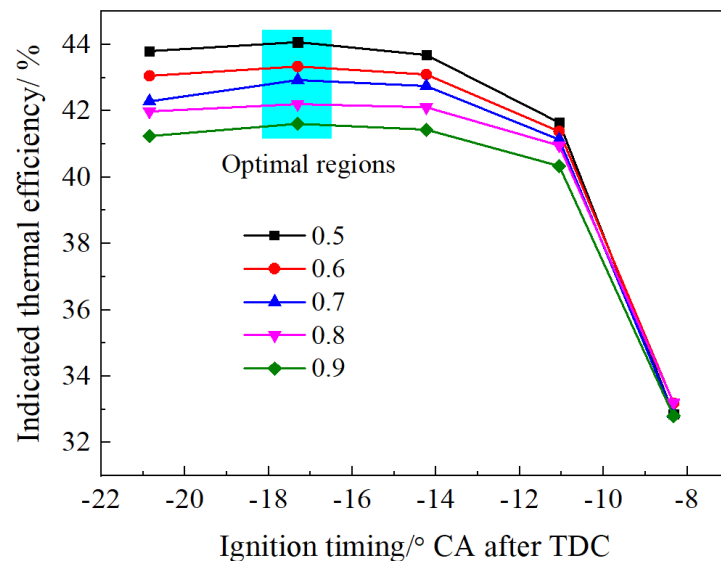


**Figure 8.** Indicated thermal efficiency over various equivalence ratios and ignition timing.

Due to the low energy density by volume of hydrogen fuel, power output of hydrogen engines was lower than that of gasoline fuel scenarios. Maximum indicated power density was approximately 15 kW/L over the engine speed of 1000 RPM and the equivalence ratio of 0.9, as shown in Figure 9. Due to the short cyclic period in time of this ORP engine, the power density of naturally aspirated ORP engine was even higher than that of turbocharged reciprocating engines over the same equivalence ratio. Brake power of a hydrogen-enriched gasoline engine increased with equivalence ratios under lean-burn conditions, regardless of the compression ratios and proportions of hydrogen additions [57].

Indicated engine torque is also shown in Figure S5. The brake engine torque reached the maximum value at an optimal ignition timing for a biogas engine, and the torque was worsened significantly when ignition timing deviated from optimal ignition timing [58]; it was also demonstrated by the research [59], the engine torque was almost linearly decreased by retarding ignition timing over the range of  $-28^{\circ}$  CA  $\sim$   $-5^{\circ}$  CA when the engine was fuelled with the blends of gasoline and 2-pheylethanol. Regarding the given ignition timing range, engine torque was sensitive to early ignition over high compression ratios; however, it was changed significantly by late ignition under low compression ratio conditions [58]. Crank angle corresponding to the maximum brake torque of a hydrogen engine was advanced by dropping equivalence ratios under wide open throttle and various engine speed conditions [60]; it was also demonstrated by the work [61], advances in ignition timing of maximum engine torque were almost linearly increased with dropping equivalence ratios, which was different with the simulation results of this ORP engine.

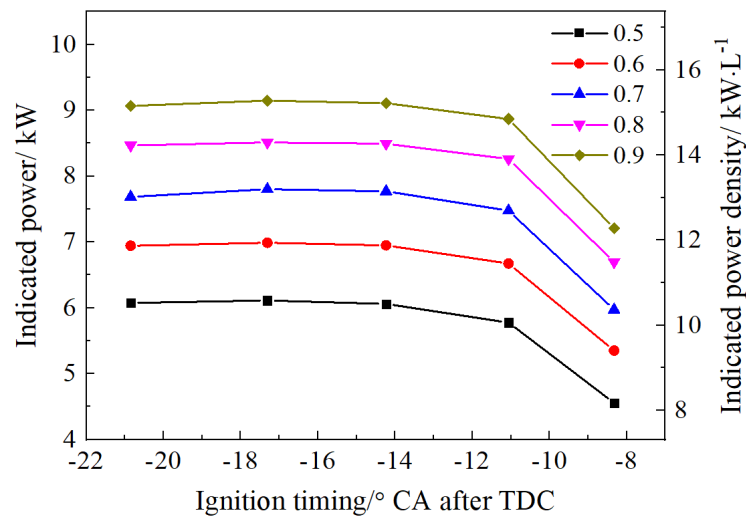


**Figure 9.** Indicated power and power density over various equivalence ratios and ignition timing.

High energy density by mass of hydrogen fuel significantly dropped the indicated specific fuel consumption (ISFC). The minimum ISFC was approximately 68 g/kWh for the given scenarios, corresponding to the equivalence ratio of 0.5 and ignition timing of  $-17.3^\circ$  CA, as indicated in Figure 10. ISFC increased approximately by 23 g/kWh when the ignition timing was retarded to  $-8.3^\circ$  CA from  $-17.3^\circ$  CA. ISFC was less dependent on the ignition timing for higher equivalence ratio scenarios. Regarding specific fuel consumption, the optimal ignition timing was around  $-25^\circ$  CA for a hydrogen-enriched spark ignition engine under 4000 RPM engine speed conditions [62]. Brake specific fuel consumption of a spark ignition engine achieved the optimal values over the equivalence ratio of 0.6~0.8 under various compression ratios and hydrogen additions conditions [57].

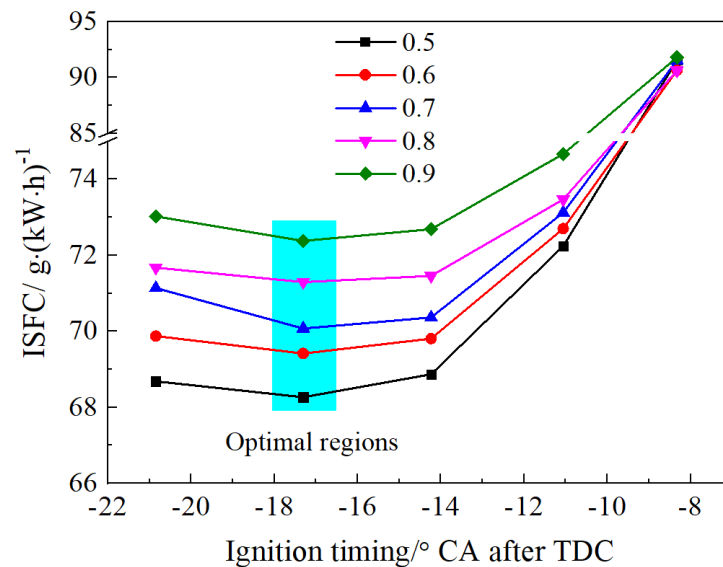


**Figure 10.** ISFC over various equivalence ratios and ignition timing.

### 3.2. Energy Loss

Combustion characteristics of hydrogen-fueled internal combustion engines changed significantly with equivalence ratios and ignition timing, leading to the variations of the energy loss by cylinder walls and exhaust. Heat loss rate profiles during the compression and expansion strokes are shown in Figure 11. Maximum heat loss rates were more dependent on the ignition timing than equivalence ratios; they were dropped from approximately 9.0 kW to 3.0 kW by retarding the ignition timing from  $-20.8^\circ$  CA to  $-8.3^\circ$  CA over the

equivalence ratio of 0.9; however, they were dropped from 9.0 kW to 5.5 kW when the equivalence ratios were dropped from 0.9 to 0.5. The heat loss by cylinder walls was determined by in-cylinder temperature which was increased by increasing equivalence ratios and advancing ignition timing (for  $-17.3^{\circ}$  CA $\sim$  $-8.3^{\circ}$  CA). At the start of compression stroke, the heat loss rates were positive which meant the heat absorptions by air-hydrogen mixture from cylinder walls.

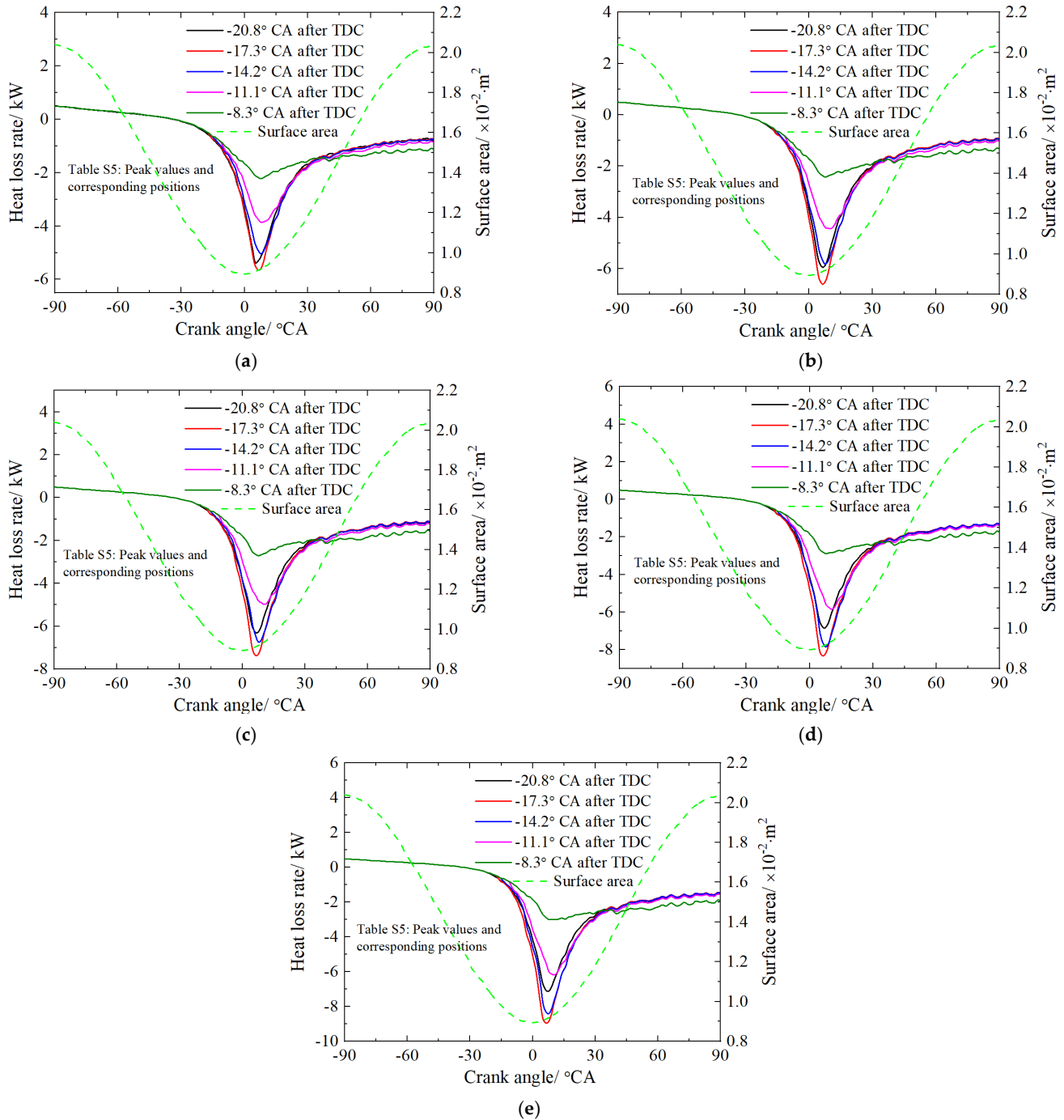


**Figure 11.** Heat loss rates by cylinder walls over various equivalence ratios and ignition timing. (a) ER: 0.5. (b) ER: 0.6. (c) ER: 0.7. (d) ER: 0.8. (e) ER: 0.9.

Total heat loss in proportions by cylinder walls is shown in Figure 12. The heat loss in proportions by cylinder walls was increased by increasing equivalence ratios, being higher than 10% for all the scenarios; ignition timing of  $-17.3^{\circ}$  CA showed the highest proportions

over individual equivalence ratios. The maximum difference of the proportions among various ignition timing was higher than 4% over the equivalence ratio of 0.9. In addition, the drop of the proportions caused by significant early ignition was the highest over the equivalence ratio of 0.9. According to the work [63], the heat loss by coolant medium in a turbocharged hydrogen engine was in the range of 20~30% of the total fuel energy under wide open throttle conditions. The proportions were much higher than this ORP engine; it was mainly caused by longer cyclic period in time of reciprocating engines than ORP engines under the same engine speed conditions. Proportions of heat loss by cylinder walls were decreased by dropping the hydrogen-air equivalence ratio. The heat loss was mainly controlled by the in-cylinder temperature. Larger hydrogen-air equivalence ratio led to high combustion temperature, further, more heat loss by cylinder walls. Ignition timing of  $-17.3^\circ$  CA had the highest in-cylinder combustion temperature, contributing to the largest heat loss by walls in proportion of chemical energy.

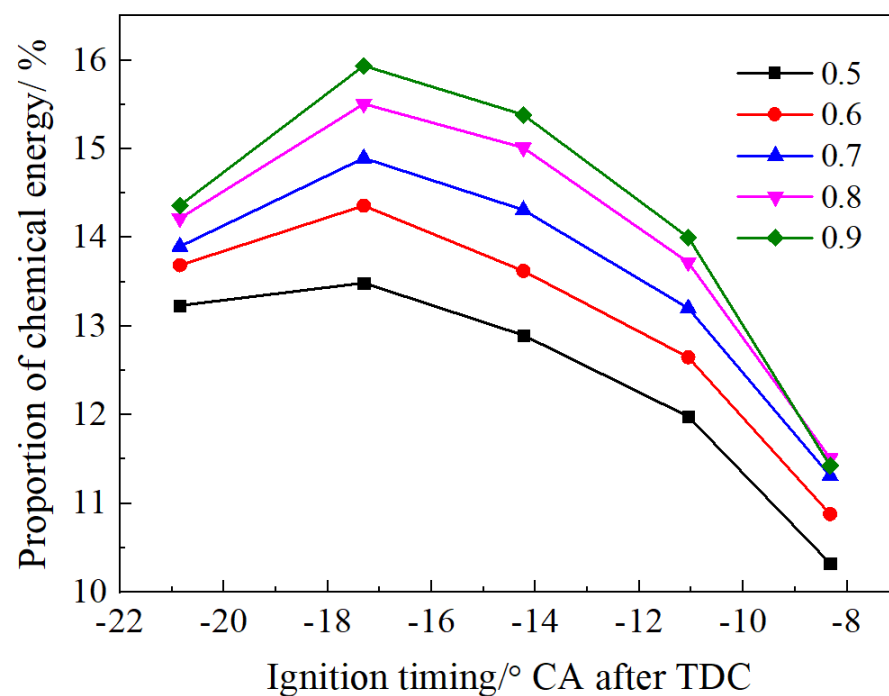


**Figure 12.** Total heat loss in proportions by cylinder walls over various equivalence ratios and ignition timing.

Energy loss proportions by exhaust over various equivalence ratios and ignition timing are shown in Figure 13. Equivalence ratios showed minor impacts on the exhaust energy loss in proportions, and the impacts were the largest among the ignition timing of  $-20.8^\circ$  CA. The energy loss in proportions by exhaust reached 56% over the ignition timing of  $-8.3^\circ$  CA, which was caused by high temperature and pressure at the end of the expansion stroke, resulting from the retarded start of combustion and prolonged combustion durations. Regarding a hydrogen-fuelled reciprocating engine, exhaust energy was lower than 35% [63] which was lower than the ORP engine. The exhaust energy loss in proportions was higher than 42% under the ignition timing of  $-17.3^\circ$  CA conditions, being corresponding to optimal indicated thermal efficiency. If the indicated thermal efficiency was kept the same, higher exhaust energy and lower coolant energy conducted to increasing the recovery efficiency of exhaust energy due to higher energy grades.

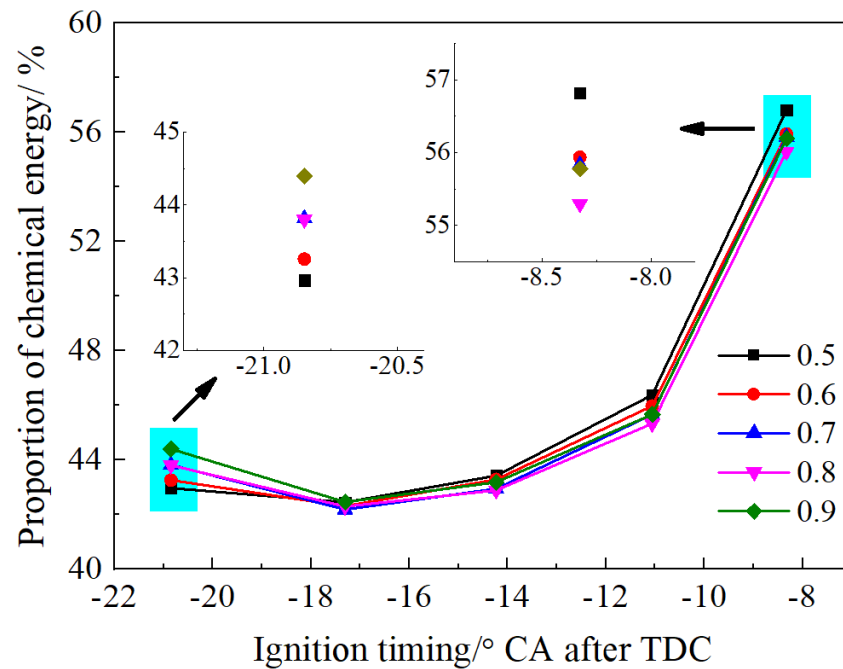


Figure 13. Energy loss in proportions by exhaust over various equivalence ratios and ignition timing.

### 3.3. $\text{NO}_x$ Emission Characteristics

Due to high combustion temperature of hydrogen fuel,  $\text{NO}_x$  emissions from hydrogen internal combustion engines were much higher than other fuels. As the main approach of dropping  $\text{NO}_x$  emissions, lean-burn technology was widely investigated [64]. Figure 14 shows  $\text{NO}_x$  concentration over various equivalence ratios and ignition timing. Since  $\text{NO}_x$  formation processes were reversible reactions,  $\text{NO}_x$  emissions remained in the burning gas were the joint impacts from forward reactions and backward reactions. Both reaction rates increased with combustion temperature.  $\text{NO}_x$  concentration evolutions are also presented in Figure S6.

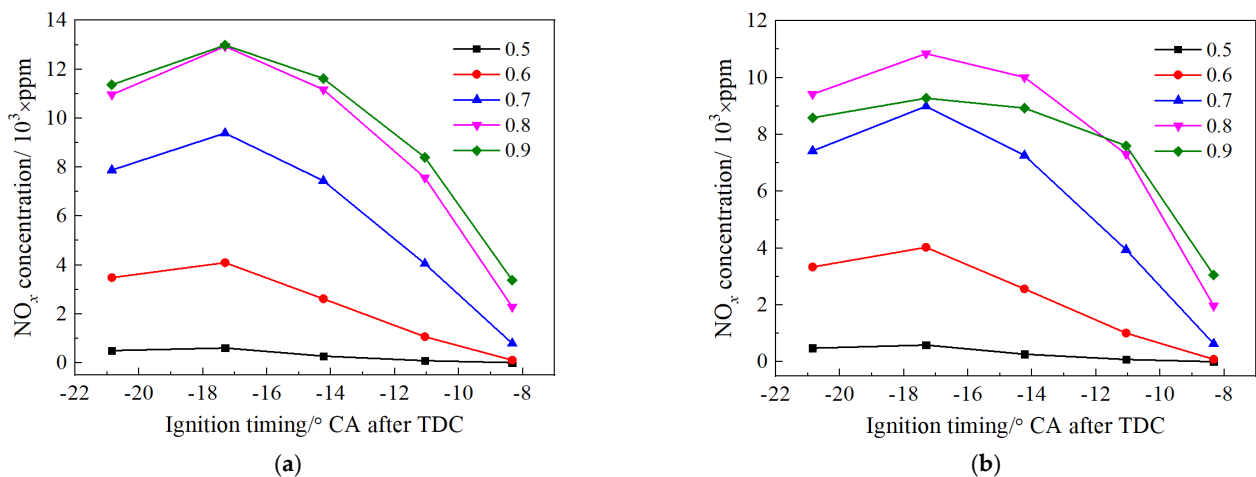


Figure 14.  $\text{NO}_x$  concentration over various equivalence ratios and ignition timing. (a) Maximum  $\text{NO}_x$  concentration. (b)  $\text{NO}_x$  concentration at the end of combustion.

Maximum  $\text{NO}_x$  concentration in the combustion process was increased by increasing equivalence ratios (see Figure 14a), due to higher combustion temperature under higher equivalence ratio conditions. Maximum and minimum values were approximately 13,000 ppm and 300 ppm, respectively. Under the same equivalence ratio conditions, maximum  $\text{NO}_x$  concentration during the combustion process corresponded to the ignition

timing of  $-17.3^\circ$  CA. Regarding  $\text{NO}_x$  concentration at the end of expansion stroke (see Figure 14b), it differed significantly from the maximum  $\text{NO}_x$  concentration during combustion. For the equivalence ratios of 0.8–0.9, low equivalence ratios led to high  $\text{NO}_x$  concentration under early ignition conditions; however, the correlations were reverse for late ignition scenarios; it was mainly caused by the significant backward reactions under the equivalence ratio of 0.8 and early ignition conditions where high in-cylinder temperature lasted long periods. Lower equivalence ratios contributed to lower  $\text{NO}_x$  concentration over various ignition timing when equivalence ratios were smaller than 0.8.  $\text{NO}_x$  formations were the combined effects from in-cylinder combustion temperature and oxygen concentration, leading to the inconsistency of  $\text{NO}_x$  concentrations with hydrogen-air equivalence ratio.

According to Hu and Huang [54],  $\text{NO}_x$  concentration was nearly increased in linear modes by advancing ignition timing over low EGR ratios for a hydrogen/natural gas engine where the maximum  $\text{NO}_x$  concentration was lower than 3000 ppm, being much lower than the authors' results. Jabbr et al. [55] indicated that the equivalence ratio of 0.8 presented the highest  $\text{NO}_x$  concentration, being higher than 10,000 ppm over the given scenarios for a hydrogen-fuelled spark ignition engine; additionally, brake thermal efficiency was dropped by the significant late ignition, agreeing well with the authors' results. According to the research [65],  $\text{NO}_x$  concentration was dropped from approximately 6800 ppm to 4000 ppm by retarding ignition timing from  $-28.75^\circ$  CA to  $-14.75^\circ$  CA for a hydrogen-enriched methane engine under 1000 RPM engine speed conditions. The effectiveness of  $\text{NO}_x$  concentration reductions by postponing ignition was lower than that of this ORP engine.

In-cylinder temperature evolutions over various equivalence ratios and ignition timing are presented in Figure 15. Peak in-cylinder combustion temperature increased with equivalence ratios over specific ignition timing. Peak in-cylinder combustion temperature increased approximately by 700 K when the equivalence ratios were increased from 0.5 to 0.9. The peak in-cylinder combustion temperature was dropped by the retarded ignition of later than  $-17.3^\circ$  CA under the given equivalence ratio conditions; additionally, the corresponding crank angle was delayed. Regarding reciprocating engines [66], peak in-cylinder temperature was increased by advancing ignition timing; however, the ORP engine presented a different pattern, resulting from the fact that significant early ignition would limit the flame developments due to the structures of ignition systems (see Figure 3). The ignition timing effects on the in-cylinder temperature at the end of expansion stroke were reverse to that of peak in-cylinder temperature. The temperature affected the proportions of exhaust energy in total fuel chemical energy. With regards to a natural gas/hydrogen Wankel engine over the equivalence ratio of 0.9 [67], the maximum in-cylinder temperature was approximately 2200 K which was much lower than this hydrogen-fuelled ORP engine.

Compared with full engine load and stoichiometric conditions [48], slightly lean-burn technology significantly promoted the  $\text{NO}_x$  formations due to more oxygen being available; additionally, the ignition timing corresponding to the highest  $\text{NO}_x$  formations was affected by engine speed [48]. In the authors' previous work [9,46,47], the ignition timing was fixed (by patching high-temperature zones) under various conditions,  $\text{NO}_x$  emission factors were lower than the results in this work; it was mainly caused by the differences in ignition timing, which was proved by the low efficiency of previous work.  $\text{NO}_x$  emission factors were less sensitive to higher equivalence ratios of 0.7–0.9. As reported by the work [57],  $\text{NO}_x$  emission factors reached the maximum value under the equivalence ratio of 0.7, and they dropped significantly by lowering equivalence ratios. According to the research [61], brake specific  $\text{NO}_x$  emission factors dropped from approximately 25 g/kWh to 2 g/kWh, achieved by increasing excess air ratios from 1.3 to 1.6 over the ignition timing of maximum brake torque.

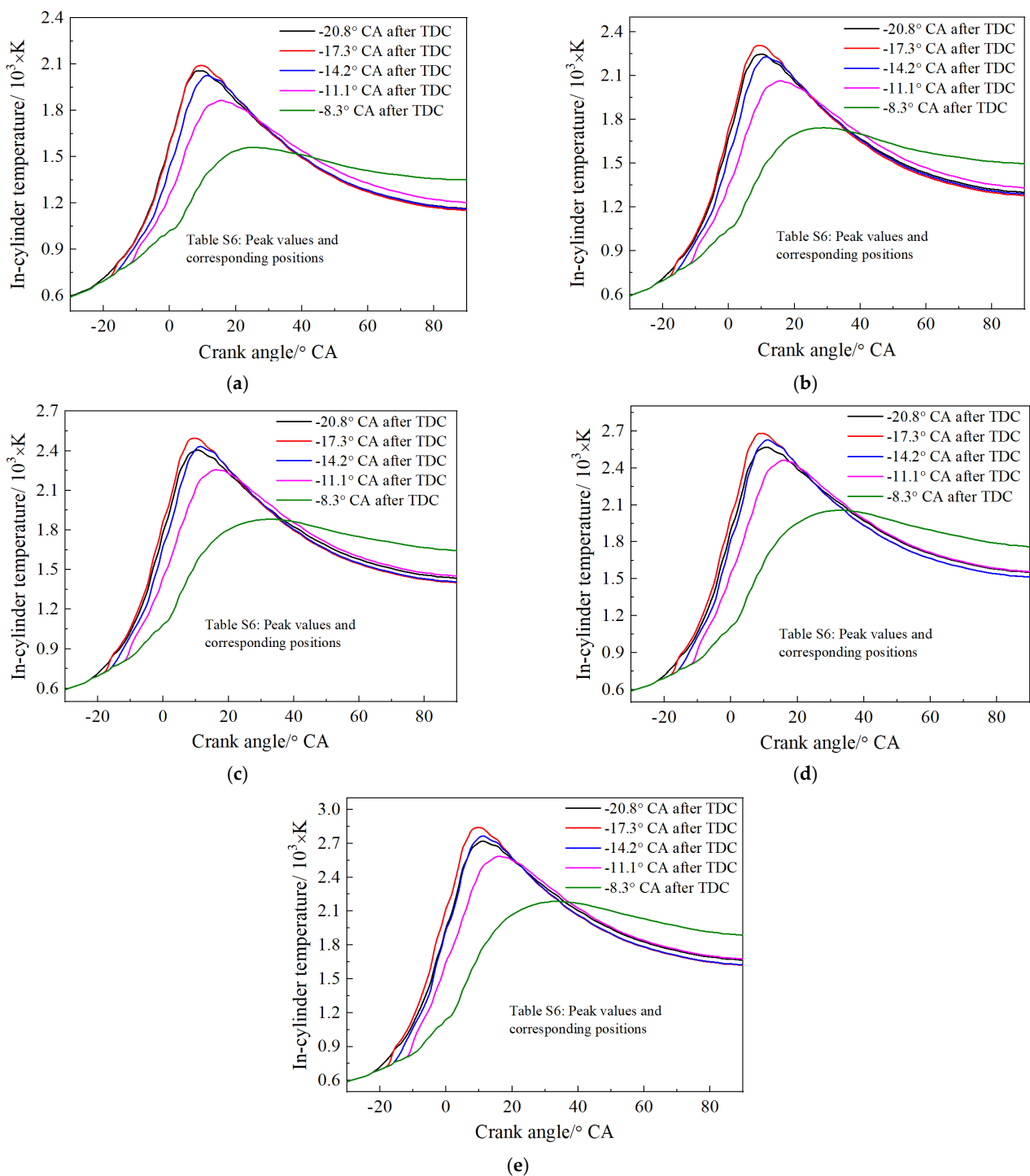


**Figure 15.** In-cylinder temperature evolutions over various equivalence ratios and ignition timing. (a) ER: 0.5. (b) ER: 0.6. (c) ER: 0.7. (d) ER: 0.8. (e) ER: 0.9.

Indicated  $NO_x$  emission factors are shown in Figure 16. Maximum  $NO_x$  emission factors were corresponding to the ignition timing of  $-17.3^\circ CA$  over individual equivalence ratio. Maximum  $NO_x$  emission factors were approximately  $43 \text{ g/kWh}$  under the equivalence ratio of 0.8; however, the minimum value was lower than  $1 \text{ g/kWh}$  under the equivalence ratio of 0.5. When the ignition timing was earlier than  $-14.2^\circ CA$ ,  $NO_x$  emission factors were dropped by lowering equivalence ratios (0.5~0.8); however, they were monotonously increased with equivalence ratios over the ignition timing of  $-8.3^\circ CA$ .

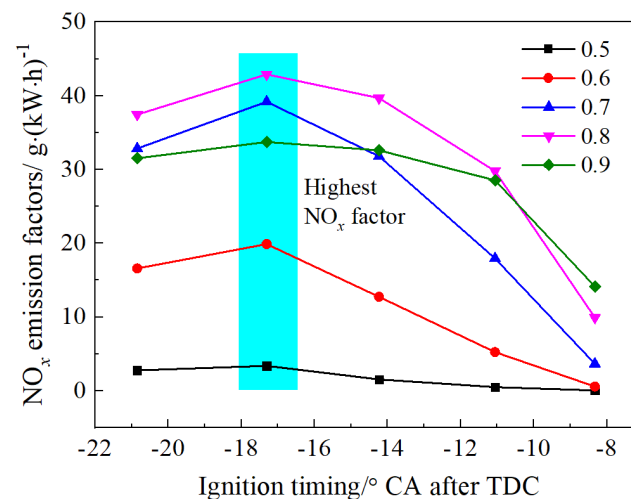


**Figure 16.** Indicated  $\text{NO}_x$  emission factors over various equivalence ratios and ignition timing.

#### 4. Conclusions

Lean-burn technology as an effective approach to mitigating  $\text{NO}_x$  emission factors was usually applied to hydrogen-fuelled internal combustion engines. Regarding engine performance of the ORP engines, the optimal ignition timing over various equivalence ratios were different from reciprocating engines. In this paper, the combustion characteristics of a hydrogen-fuelled ORP engine over various equivalence ratios and ignition timing were investigated; meantime, the energy loss and  $\text{NO}_x$  emissions were explored. The main findings from this research are as the follows:

- (1) Peak in-cylinder pressure was significantly dependent on the equivalence ratios and ignition timing. The value was increased approximately by 13 bar when the equivalence ratios were increased from 0.5 to 0.9. Crank angle corresponding to the peak in-cylinder pressure was slightly dependent on the ignition timing for individual equivalence ratios. Peak in-cylinder pressure was more sensitive to late ignition than early ignition. Discharge pressure was increased by increasing equivalence ratios over the same ignition timing; however, it showed minor difference over the ignition timing of  $-17.3^\circ \text{ CA} \sim -14.2^\circ \text{ CA}$  under the same equivalence ratio conditions. Special relative positions of the ignition systems to combustion chambers led to the different in-cylinder pressure evolutions from reciprocating engines under early ignition conditions.
- (2) The start of combustion, combustion phase, and combustion durations presented parabolic shapes with ignition timing, with the minimum value being around the ignition timing of  $-17.3^\circ \text{ CA}$  over individual equivalence ratios. Regarding the specific equivalence ratios, start of combustion was advanced by early ignition; however, the impacts on combustion phase and combustion durations were inconsistent by ignition timing. Maximum heat release rates were changed slightly by the ignition timing of  $-20.8^\circ \text{ CA} \sim -14.2^\circ \text{ CA}$  for the individual equivalence ratios; and the values decreased significantly for late ignition scenarios.
- (3) The optimal indicated thermal efficiency was higher than 41% for the equivalence ratios of 0.5~0.9. Indicated thermal efficiency showed minor dependency on the ignition timing for early ignition scenarios; however, the decrease was more than 10% for the ignition timing of  $-8.3^\circ \text{ CA}$  compared with the optimal efficiency. The minimum ISFC was lower than 68.5 g/kWh, corresponding to the equivalence ratio of 0.5 and ignition timing of  $-17.3^\circ \text{ CA}$ .
- (4) Heat loss in proportions of total fuel energy by cylinder walls increased with equivalence ratios. The relationships between the proportions and ignition timing were in parabolic shapes, with the maximum value corresponding to the ignition timing of

–17.3° CA. Equivalence ratios showed minor impacts on the heat loss in proportions of total fuel energy by the exhaust.

- (5) Peak NO<sub>x</sub> concentration during combustion increased with equivalence ratios; however, the patterns depended on the ignition timing for NO<sub>x</sub> concentration at the end of expansion stroke due to the severe effects from reverse reactions during NO<sub>x</sub> formations. The maximum NO<sub>x</sub> emission factor was approximately 43 g/kWh under the equivalence ratio of 0.8; however, the minimum value was lower than 1 g/kWh under the equivalence ratio of 0.5.

Due to the applications of hydrogen port injection and lean-burn technology, the power density of the ORP engine was dropped significantly compared with gasoline scenarios due to less fuel energy delivery; the combination effect of hydrogen direct injection (DI) and ignition timing will be investigated in the authors' future work to increase the power density and thermal efficiency; in addition, the optimal hydrogen injection strategies will be explored, and the existing of the cylinder bowls can make it different from the conventional engines.

**Supplementary Materials:** The following supporting information can be downloaded at: <https://www.mdpi.com/article/10.3390/pr10081534/s1>.

**Author Contributions:** J.G. and J.H.: Formal analysis, Investigation, Methodology, Resources, Validation, Visualization, Writing—original draft, Writing—review and editing. G.T.: Conceptualization, Funding acquisition, Methodology, Project administration, Resources, Software, Supervision, Visualization, Writing—review and editing. C.M.: Investigation, Writing review and editing; C.Y.: Visualization, Writing—review and editing, Supervision. All authors have read and agreed to the published version of the manuscript.

**Funding:** The research reported in this paper was supported by “Beijing Institute of Technology Research Fund Program for Young Scholars (XSQD-202203001)”, “the Fundamental Research Funds for the Central Universities, CHD (300102222509, 300102222104)”, and National Natural Science Foundation of China (Grant No. 51736001).

**Institutional Review Board Statement:** Not applicable.

**Informed Consent Statement:** Not applicable.

**Data Availability Statement:** The data will be provided if requested.

**Acknowledgments:** The authors would like to acknowledge the Enigma England Ltd. for providing the 3D model of the ORP engine.

**Conflicts of Interest:** The authors declare that they have no known competing financial interest or personal relationships that could have appeared to influence the work reported in this paper.

## Nomenclature

BDCs	bottom dead centres
BSFC	brake specific fuel consumption
CA	crank angle
CO	carbon monoxide
CO <sub>2</sub>	carbon dioxide
DI	direct injection
EGR	exhaust gas recirculation
HC	hydrocarbon
ISFC	indicated specific fuel consumption
NO <sub>x</sub>	nitrogen oxides
ORP	opposed rotary piston
RNG	Re-Normalisation Group
TDCs	top dead centres

## References

1. Kojima, N.; Tokai, A.; Nakakubo, T.; Nagata, Y. Policy evaluation of vehicle exhaust standards in Japan from 1995 to 2005 based on two human health risk indices for air pollution and global warming. *Environ. Syst. Decis.* **2016**, *36*, 229–238. [[CrossRef](#)]
2. Acar, C.; Dincer, I. The potential role of hydrogen as a sustainable transportation fuel to combat global warming. *Int. J. Hydrogen Energy* **2020**, *45*, 3396–3406. [[CrossRef](#)]
3. Buckeridge, D.L.; Glazier, R.; Harvey, B.J.; Escobar, M.; Amrhein, C.; Frank, J.W. Effect of motor vehicle emissions on respiratory health in an urban area. *Environ. Health Perspect.* **2002**, *110*, 293–300. [[CrossRef](#)] [[PubMed](#)]
4. Gao, J.; Tian, G.; Sornioti, A.; Karci, A.E.; Di Palo, R. Review of thermal management of catalytic converters to decrease engine emissions during cold start and warm up. *Appl. Therm. Eng.* **2019**, *147*, 177–187. [[CrossRef](#)]
5. Wolfram, P.; Wiedmann, T. Electrifying Australian transport: Hybrid life cycle analysis of a transition to electric light-duty vehicles and renewable electricity. *Appl. Energy* **2017**, *206*, 531–540. [[CrossRef](#)]
6. Gökce, K.; Ozdemir, A. An instantaneous optimization strategy based on efficiency maps for internal combustion engine/battery hybrid vehicles. *Energy Convers. Manag.* **2014**, *81*, 255–269. [[CrossRef](#)]
7. Sadiq, G.A.; Al-Dadah, R.; Mahmoud, S. Development of rotary Wankel devices for hybrid automotive applications. *Energy Convers. Manag.* **2019**, *202*, 112159. [[CrossRef](#)]
8. Gao, J.; Tian, G.; Ma, C.; Xing, S.; Jenner, P. Performance explorations of a naturally aspirated opposed rotary piston engine fuelled with hydrogen under part load and stoichiometric conditions using a numerical simulation approach. *Energy* **2021**, *222*, 120003. [[CrossRef](#)]
9. Gao, J.; Tian, G.; Ma, C.; Balasubramanian, D.; Xing, S.; Jenner, P. Numerical investigations of combustion and emissions characteristics of a novel small scale opposed rotary piston engine fuelled with hydrogen at wide open throttle and stoichiometric conditions. *Energy Convers. Manag.* **2020**, *221*, 113178. [[CrossRef](#)]
10. Gong, C.; Yi, L.; Zhang, Z.; Sun, J.; Liu, F. Assessment of ultra-lean burn characteristics for a stratified-charge direct-injection spark-ignition methanol engine under different high compression ratios. *Appl. Energy* **2020**, *261*, 114478. [[CrossRef](#)]
11. Chen, W.; Pan, J.; Zuo, Q.; Zhang, J.; Wang, Z.; Zhang, B.; Zhu, G.; Fan, B. Combustion performance improvement of a diesel fueled Wankel stratified-charge combustion engine by optimizing assisted ignition strategy. *Energy Convers. Manag.* **2020**, *205*, 112324. [[CrossRef](#)]
12. Qian, Y.; Wang, J.; Li, Z.; Jiang, C. Improvement of combustion performance and emissions in a gasoline direct injection (GDI) engine by modulation of fuel volatility. *Fuel* **2020**, *268*, 117369. [[CrossRef](#)]
13. Gong, C.; Sun, J.; Liu, F. Numerical study of twin-spark plug arrangement effects on flame, combustion and emissions of a medium compression ratio direct-injection methanol engine. *Fuel* **2020**, *279*, 118427. [[CrossRef](#)]
14. Amrouche, F.; Erickson, P.; Park, J.; Varnhagen, S. An experimental evaluation of ultra-lean burn capability of a hydrogen-enriched ethanol-fuelled Wankel engine at full load condition. *Int. J. Hydrogen Energy* **2016**, *41*, 19231–19242. [[CrossRef](#)]
15. Su, T.; Ji, C.; Wang, S.; Shi, L.; Yang, J.; Cong, X. Reducing the idle speed of a gasoline rotary engine with hydrogen addition. *Int. J. Hydrogen Energy* **2017**, *42*, 23218–23226. [[CrossRef](#)]
16. Shi, C.; Ji, C.; Wang, S.; Yang, J.; Li, X.; Ge, Y. Effects of hydrogen direct-injection angle and charge concentration on gasoline-hydrogen blending lean combustion in a Wankel engine. *Energy Convers. Manag.* **2019**, *187*, 316–327. [[CrossRef](#)]
17. Ozcanli, M.; Bas, O.; Akar, M.A.; Yildizhan, S.; Serin, H. Recent studies on hydrogen usage in Wankel SI engine. *Int. J. Hydrogen Energy* **2018**, *43*, 18037–18045. [[CrossRef](#)]
18. Chen, H.; Pan, C.-Y.; Xu, H.-J.; Deng, H.; Han, C. Analysis on structural characteristics of rotors in twin-rotor cylinder-embedded piston engine. *J. Cent. South Univ.* **2014**, *21*, 2240–2252. [[CrossRef](#)]
19. Zou, T.-A.; Xu, H.-J.; Pan, C.-Y.; Xu, X.-J.; Chen, H. Mathematical modeling and analysis of thermodynamic processes in a twin-rotor piston engine. *J. Cent. South Univ.* **2014**, *21*, 4163–4171. [[CrossRef](#)]
20. Pan, D.; Xu, H.; Liu, B.; Yang, C. Research on sealing characteristics of annular power cylinder based on twin-rotor piston engine. *Proc. Inst. Mech. Eng. Part C J. Mech. Eng. Sci.* **2021**, *236*, 09544062211021440. [[CrossRef](#)]
21. Gao, J.; Tian, G.; Jenner, P.; Burgess, M.; Emhardt, S. Preliminary explorations of the performance of a novel small scale opposed rotary piston engine. *Energy* **2020**, *190*, 116402. [[CrossRef](#)]
22. You, J.; Liu, Z.; Wang, Z.; Wang, D.; Xu, Y. Impact of natural gas injection strategies on combustion and emissions of a dual fuel natural gas engine ignited with diesel at low loads. *Fuel* **2020**, *260*, 116414. [[CrossRef](#)]
23. Pastor, J.V.; García, A.; Micó, C.; García-Carrero, A.A. Experimental study of influence of Liquefied Petroleum Gas addition in Hydrotreated Vegetable Oil fuel on ignition delay, flame lift off length and soot emission under diesel-like conditions. *Fuel* **2020**, *260*, 116377. [[CrossRef](#)]
24. Verhelst, S.; Turner, J.W.; Sileghem, L.; Vancoillie, J. Methanol as a fuel for internal combustion engines. *Prog. Energy Combust. Sci.* **2019**, *70*, 43–88. [[CrossRef](#)]
25. Gong, C.; Zhang, Z.; Sun, J.; Chen, Y.; Liu, F. Computational study of nozzle spray-line distribution effects on stratified mixture formation, combustion and emissions of a high compression ratio DISI methanol engine under lean-burn condition. *Energy* **2020**, *205*, 118080. [[CrossRef](#)]
26. Del Pecchia, M.; Pessina, V.; Berni, F.; d’Adamo, A.; Fontanesi, S. Gasoline-ethanol blend formulation to mimic laminar flame speed and auto-ignition quality in automotive engines. *Fuel* **2020**, *264*, 116741. [[CrossRef](#)]

27. Rajak, U.; Nashine, P.; Verma, T.N. Characteristics of microalgae spirulina biodiesel with the impact of n-butanol addition on a CI engine. *Energy* **2019**, *189*, 116311. [\[CrossRef\]](#)
28. Şanlı, B.G.; Uludamar, E.; Özcanlı, M. Evaluation of energetic-exergetic and sustainability parameters of biodiesel fuels produced from palm oil and opium poppy oil as alternative fuels in diesel engines. *Fuel* **2019**, *258*, 116116. [\[CrossRef\]](#)
29. Chan, J.; Tsolakis, A.; Herreros, J.; Kallis, K.; Hergueta, C.; Sittichompoo, S.; Bogarra, M. Combustion, gaseous emissions and PM characteristics of Di-Methyl Carbonate (DMC)-gasoline blend on gasoline Direct Injection (GDI) engine. *Fuel* **2020**, *263*, 116742. [\[CrossRef\]](#)
30. Gao, J.; Wang, X.; Song, P.; Tian, G.; Ma, C. Review of the backfire occurrences and control strategies for port hydrogen injection internal combustion engines. *Fuel* **2022**, *307*, 121553. [\[CrossRef\]](#)
31. Boretti, A. Hydrogen internal combustion engines to 2030. *Int. J. Hydrogen Energy* **2020**, *45*, 23692–23703. [\[CrossRef\]](#)
32. Cho, E.S.; Ruminiski, A.M.; Aloni, S.; Liu, Y.-S.; Guo, J.; Urban, J.J. Graphene oxide/metal nanocrystal multilaminates as the atomic limit for safe and selective hydrogen storage. *Nat. Commun.* **2016**, *7*, 10804. [\[CrossRef\]](#) [\[PubMed\]](#)
33. Ishii, M.; Wakai, S. *Electron-Based Bioscience and Biotechnology*; Springer: Berlin/Heidelberg, Germany, 2020; pp. 81–99.
34. Akal, D.; Öztuna, S.; Büyükkakın, M.K. A review of hydrogen usage in internal combustion engines (gasoline-Lpg-diesel) from combustion performance aspect. *Int. J. Hydrogen Energy* **2020**, *45*, 35257–35268. [\[CrossRef\]](#)
35. Gürbüz, H.; Akçay, İ.H. Evaluating the effects of boosting intake-air pressure on the performance and environmental-economic indicators in a hydrogen-fueled SI engine. *Int. J. Hydrogen Energy* **2021**, *46*, 28801–28810. [\[CrossRef\]](#)
36. Shi, C.; Ji, C.; Wang, S.; Yang, J.; Li, X.; Ge, Y. Numerical simulation on combustion process of a hydrogen direct-injection stratified gasoline Wankel engine by synchronous and asynchronous ignition modes. *Energy Convers. Manag.* **2019**, *183*, 14–25. [\[CrossRef\]](#)
37. Su, T.; Ji, C.; Wang, S.; Cong, X.; Shi, L.; Yang, J. Improving the lean performance of an n-butanol rotary engine by hydrogen enrichment. *Energy Convers. Manag.* **2018**, *157*, 96–102. [\[CrossRef\]](#)
38. Gong, C.; Li, Z.; Yi, L.; Liu, F. Comparative study on combustion and emissions between methanol port-injection engine and methanol direct-injection engine with H<sub>2</sub>-enriched port-injection under lean-burn conditions. *Energy Convers. Manag.* **2019**, *200*, 112096. [\[CrossRef\]](#)
39. Gong, C.; Li, Z.; Yi, L.; Sun, J.; Liu, F. Comparative analysis of various combustion phase control methods in a lean-burn H<sub>2</sub>/methanol fuel dual-injection engine. *Fuel* **2020**, *262*, 116592. [\[CrossRef\]](#)
40. Du, Y.; Yu, X.; Liu, L.; Li, R.; Zuo, X.; Sun, Y. Effect of addition of hydrogen and exhaust gas recirculation on characteristics of hydrogen gasoline engine. *Int. J. Hydrogen Energy* **2017**, *42*, 8288–8298. [\[CrossRef\]](#)
41. Gong, C.; Li, Z.; Huang, K.; Liu, F. Research on the performance of a hydrogen/methanol dual-injection assisted spark-ignition engine using late-injection strategy for methanol. *Fuel* **2020**, *260*, 116403. [\[CrossRef\]](#)
42. Gong, C.; Li, Z.; Sun, J.; Liu, F. Evaluation on combustion and lean-burn limit of a medium compression ratio hydrogen/methanol dual-injection spark-ignition engine under methanol late-injection. *Appl. Energy* **2020**, *277*, 115622. [\[CrossRef\]](#)
43. Yu, X.; Du, Y.; Sun, P.; Liu, L.; Wu, H.; Zuo, X. Effects of hydrogen direct injection strategy on characteristics of lean-burn hydrogen-gasoline engines. *Fuel* **2017**, *208*, 602–611. [\[CrossRef\]](#)
44. Shi, C.; Ji, C.; Ge, Y.; Wang, S.; Yang, J.; Wang, H. Effects of split direct-injected hydrogen strategies on combustion and emissions performance of a small-scale rotary engine. *Energy* **2021**, *215*, 119124. [\[CrossRef\]](#)
45. Gao, J.; Xing, S.; Tian, G.; Ma, C.; Zhao, M.; Jenner, P. Numerical simulation on the combustion and NO<sub>x</sub> emission characteristics of a turbocharged opposed rotary piston engine fuelled with hydrogen under wide open throttle conditions. *Fuel* **2021**, *285*, 119210. [\[CrossRef\]](#)
46. Gao, J.; Tian, G.; Ma, C.; Xing, S.; Jenner, P. Lean-burn characteristics of a turbocharged opposed rotary piston engine fuelled with hydrogen at low engine speed conditions. *Int. J. Hydrogen Energy* **2021**, *46*, 1219–1233. [\[CrossRef\]](#)
47. Gao, J.; Tian, G.; Ma, C.; Xing, S.; Huang, L. Numerical simulation on lean-burn characteristics of a naturally aspirated opposed rotary piston engine fuelled with hydrogen at wide open throttle conditions. *J. Clean. Prod.* **2021**, *285*, 124887. [\[CrossRef\]](#)
48. Gao, J.; Tian, G.; Ma, C.; Xing, S.; Huang, L. Three-dimensional numerical simulations on the effect of ignition timing on combustion characteristics, nitrogen oxides emissions, and energy loss of a hydrogen fuelled opposed rotary piston engine over wide open throttle conditions. *Fuel* **2021**, *288*, 119722. [\[CrossRef\]](#)
49. Gao, J.; Tian, G.; Ma, C.; Xing, S.; Huang, L. Explorations of the impacts on a hydrogen fuelled opposed rotary piston engine performance by ignition timing under part load conditions. *Int. J. Hydrogen Energy* **2021**, *46*, 11994–12008. [\[CrossRef\]](#)
50. ANSYS. *ANSYS Fluent Theory Guide*; ANSYS: Canonsburg, PA, USA, 2013.
51. Chapter 17: Modeling Pollutant Formation. In *FLUENT*; FLUENT, Inc.: New York, NY, USA, 2001.
52. Luo, Q.-H.; Hu, J.-B.; Sun, B.-G.; Liu, F.-S.; Wang, X.; Li, C.; Bao, L.-Z. Experimental investigation of combustion characteristics and NO<sub>x</sub> emission of a turbocharged hydrogen internal combustion engine. *Int. J. Hydrogen Energy* **2019**, *44*, 5573–5584. [\[CrossRef\]](#)
53. Arroyo, J.; Moreno, F.; Muñoz, M.; Monné, C. Experimental study of ignition timing and supercharging effects on a gasoline engine fueled with synthetic gases extracted from biogas. *Energy Convers. Manag.* **2015**, *97*, 196–211. [\[CrossRef\]](#)
54. Hu, E.; Huang, Z. *Optimization on Ignition Timing and EGR Ratio of a Spark-Ignition Engine Fuelled with Natural Gas-Hydrogen Blends*; SAE Technical Paper Report No. 0148-7191; SAE: Detroit, MI, USA, 2011.
55. Jabbr, A.I.; Vaz, W.S.; Khairallah, H.A.; Koylu, U.O. Multi-objective optimization of operating parameters for hydrogen-fueled spark-ignition engines. *Int. J. Hydrogen Energy* **2016**, *41*, 18291–18299. [\[CrossRef\]](#)

56. Sari, R.; Golke, D.; Enzweiler, H.; Salau, N.; Pereira, F.; Martins, M. Exploring optimal operating conditions for wet ethanol use in spark ignition engines. *Appl. Therm. Eng.* **2018**, *138*, 523–533. [[CrossRef](#)]
57. Bhasker, J.P.; Porpatham, E. Effects of compression ratio and hydrogen addition on lean combustion characteristics and emission formation in a Compressed Natural Gas fuelled spark ignition engine. *Fuel* **2017**, *208*, 260–270. [[CrossRef](#)]
58. Hotta, S.K.; Sahoo, N.; Mohanty, K.; Kulkarni, V. Ignition timing and compression ratio as effective means for the improvement in the operating characteristics of a biogas fueled spark ignition engine. *Renew. Energy* **2020**, *150*, 854–867. [[CrossRef](#)]
59. Pan, M.; Wei, H.; Feng, D.; Pan, J.; Huang, R.; Liao, J. Experimental study on combustion characteristics and emission performance of 2-phenylethanol addition in a downsized gasoline engine. *Energy* **2018**, *163*, 894–904. [[CrossRef](#)]
60. Ortiz-Imedio, R.; Ortiz, A.; Urroz, J.; Diéguez, P.; Gorri, D.; Gandía, L.; Ortiz, I. Comparative performance of coke oven gas, hydrogen and methane in a spark ignition engine. *Int. J. Hydrogen Energy* **2020**, *46*, 17572–17586. [[CrossRef](#)]
61. Ma, F.; Wang, Y.; Liu, H.; Li, Y.; Wang, J.; Ding, S. Effects of hydrogen addition on cycle-by-cycle variations in a lean burn natural gas spark-ignition engine. *Int. J. Hydrogen Energy* **2008**, *33*, 823–831. [[CrossRef](#)]
62. Zareei, J.; Rohani, A. Optimization and study of performance parameters in an engine fueled with hydrogen. *Int. J. Hydrogen Energy* **2020**, *45*, 322–336. [[CrossRef](#)]
63. Wang, X.; Sun, B.-G.; Luo, Q.-H. Energy and exergy analysis of a turbocharged hydrogen internal combustion engine. *Int. J. Hydrogen Energy* **2019**, *44*, 5551–5563. [[CrossRef](#)]
64. He, B.-Q.; Xu, S.-P.; Fu, X.-Q.; Zhao, H. Combustion and emission characteristics of an ultra-lean burn gasoline engine with dimethyl ether auto-ignition. *Energy* **2020**, *209*, 118437. [[CrossRef](#)]
65. Duan, X.; Li, Y.; Liu, J.; Guo, G.; Fu, J.; Zhang, Q.; Zhang, S.; Liu, W. Experimental study the effects of various compression ratios and spark timing on performance and emission of a lean-burn heavy-duty spark ignition engine fueled with methane gas and hydrogen blends. *Energy* **2019**, *169*, 558–571. [[CrossRef](#)]
66. Nuthan, P.B.S.; Kumar, G.N. Influence of ignition timing on performance and emission characteristics of an SI engine fueled with equi-volume blend of methanol and gasoline. *Energy Sources Part A Recovery Util. Environ. Eff.* **2019**, 1–15. [[CrossRef](#)]
67. Fan, B.; Zhang, Y.; Pan, J.; Liu, Y.; Chen, W.; Otchere, P.; Wei, A.; He, R. The influence of hydrogen injection strategy on mixture formation and combustion process in a port injection (PI) rotary engine fueled with natural gas/hydrogen blends. *Energy Convers. Manag.* **2018**, *173*, 527–538. [[CrossRef](#)]